

Polymer Chemistry

Accepted Manuscript

This article can be cited before page numbers have been issued, to do this please use: M. T. T. Gace, E. C. Quinn, F. Shariatikia, J. L. Olmedo-Martínez, S. Xu, A. J. Muller and E. Y.-X. Chen, *Polym. Chem.*, 2025, DOI: 10.1039/D5PY00691K.



This is an Accepted Manuscript, which has been through the Royal Society of Chemistry peer review process and has been accepted for publication.

Accepted Manuscripts are published online shortly after acceptance, before technical editing, formatting and proof reading. Using this free service, authors can make their results available to the community, in citable form, before we publish the edited article. We will replace this Accepted Manuscript with the edited and formatted Advance Article as soon as it is available.

You can find more information about Accepted Manuscripts in the [Information for Authors](#).

Please note that technical editing may introduce minor changes to the text and/or graphics, which may alter content. The journal's standard [Terms & Conditions](#) and the [Ethical guidelines](#) still apply. In no event shall the Royal Society of Chemistry be held responsible for any errors or omissions in this Accepted Manuscript or any consequences arising from the use of any information it contains.

ARTICLE

Synergistic engineering of poly(3-hydroxybutyrate) architecture and stereomicrostructure achieves enhanced material properties

Maëlle T. Gace^a, Ethan C. Quinn^a, Fateme Shariatikia^b, Jorge L. Olmedo-Martínez^b, Shu Xu^c, Alejandro J. Müller^{b,d,*}, and Eugene Y.-X. Chen^{a,*}Received 00th January 20xx,
Accepted 00th January 20xx

DOI: 10.1039/x0xx00000x

Chemically engineering stereomicrostructures of biodegradable poly(3-hydroxybutyrate) (P3HB) has shown to be an effective approach to largely modulate its properties towards mono-material product design, but whether coupling of this method with engineering P3HB architectures could yield an even more effective strategy has yet to be demonstrated. Here, through the stereochemically and architecturally controlled polymerization, four-arm star-shaped P3HBs consisting of stereo-perfect isotactic, iso-rich, and syndio-rich stereomicrostructures, as well as their linear counterparts of comparable molar mass as controls, have been synthesized. Comprehensive and comparative characterization studies have uncovered various degrees of impacts of the P3HB architecture on thermal transitions and crystallization behaviors, mechanical performance, as well as rheological and gas barrier properties. In particular, coupling of both stereomicrostructure and architecture engineering approaches has produced synergistically enhanced effects on the overall materials properties, providing a more powerful strategy to design mono-materials with vastly different properties without changing their chemical composition.

Introduction

Over the past century and a half, the development of synthetic polymers from petroleum byproducts has revolutionized industries by providing cost-effective, durable, and high-performance plastics.^{1–7} Despite their essential role in society, the prevailing approach to designing and producing plastics has followed a linear economy model, often failing to address sustainable end-of-life options.^{8,9} The urgent challenge we now face is to find sustainable alternatives to petroleum-based, nondegradable plastics to mitigate the global plastics crisis. One promising approach involves synthesizing biobased and biodegradable plastics.^{10–14}

Polyhydroxyalkanoates (PHAs) – a class of natural polyesters produced by bacteria and other microorganisms – emerge as a promising solution to address this demand for biobased plastics. Renowned for their ability to degrade in managed and unmanaged conditions, alongside their tunable thermal and mechanical properties, PHAs present an attractive alternative to petroleum-based commodity plastics.^{15–22} Among PHAs, biologically produced, isotactic P3HB (*it*-P3HB_b) exhibits perfect

isotacticity with an absolute (*R*)-stereoconfiguration and is a highly crystalline material with a high melting temperature (T_m) of ~175 °C. It shows good barrier properties and a high tensile strength, but it is highly brittle (elongation at break (ϵ_B) ~3–5%) and possesses a narrow processing window (due to its low decomposition temperature (T_d) ~250 °C).^{17,23,24} Despite significant advancements in engineering PHAs metabolic pathways, the biosynthetic route remains constrained by microstructural and architectural complexity limitations.^{25–29}

Since the 1960s, significant research has focused on the ring-opening polymerization (ROP) of lactones to create synthetic analogs of *it*-P3HB_b.³⁰ The simplest monomer for producing P3HB is the highly strained, four-membered β -butyrolactone (BBL). Although BBL has been extensively studied, achieving highly to quantitatively isotactic P3HB materials has been challenging. Historically, polymerizations of a *racemic* mixture of BBL have shown limited success, yielding polymers with a P_m (probability of *meso* linkages between monomer units) of ≤ 0.92 .^{31–40} This limitation arises from the small, flat monomer structure and the polymerization pathways involving both alkyl and acyl cleavages, which impairs the ability of achieving high control and isotacticity or utilizing less stereoselective catalysts.^{17,41,42} Recently, studies have demonstrated that lowering the temperature to 0 °C or even to -35 °C, or using enantiopure catalysts can increase isoselectivity.^{40,43,44} Seeking an alternative route, we developed a method to synthetically produce isotactic P3HB (*it*-P3HB_s) with $P_m > 0.99$ by employing the ROP of the *racemic* eight-membered dimethyl diolide (*rac*-8DL^{Me}) with C_2 -chiral salen-based metal complexes.⁴⁵

The 8DL^{Me} platform was then extended in efforts to enhance the toughness of *it*-P3HB through a range of strategies. These efforts included copolymerizing *rac*-8DL^{Me} with 8DL^R (R = Et, ⁿBu,

^a Department of Chemistry, Colorado State University, Fort Collins, CO 80523-1872, United States.

^b POLYMAT and Department of Polymers and Advanced Materials: Physics, Chemistry and Technology, Faculty of Chemistry, University of the Basque Country UPV/EHU, Donostia-San Sebastián 20018, Spain.

^c Applied Materials Division, Argonne National Laboratory, Lemont, IL 60439, USA

^d IKERBASQUE, Basque Foundation for Science, Plaza Euskadi 5, Bilbao 48009, Spain.

* Footnotes relating to the title and/or authors should appear here.

Supplementary Information available: [details of any supplementary information available should be included here]. See DOI: 10.1039/x0xx00000x



Bn) or other lactones,^{46–51} engineering its stereomicrostructure,⁵² implementing blending strategies,⁵³ exploring block architectures,^{46,54} alternating *it*-PHAs,⁵⁵ and designing α,α -disubstituted PHAs.⁵⁶ Consequently, a diverse array of PHA materials emerged, spanning from strong yet brittle thermoplastics to ductile and tough thermoplastics and elastomers. It should be pointed out that, although the copolymerization approaches successfully toughened *it*-P3HB, they increase the synthetic and chemical complexity, complicating possible mechanical and chemical recycling routes and hampering the possibility of creating mono-material products.⁵⁷

Commercial plastic products typically require multiple materials to function and adhere to common application standards, especially packaging.^{57–59} However, recycling these multi-layer products is challenging and energy-intensive due to their immiscibility and/or different chemical compositions. These significant issues contribute to the rising demand for single-monomer sourced mono-material product design as a more sustainable approach. Utilizing the stereomicrostructural engineering approach makes it possible to produce customized properties using a single monomer.⁵²

Another method central to this study involves the engineering of P3HB's architecture. It has been shown that the physical properties of polymers can be modulated through architectural engineering, providing a means to achieve desired properties.^{60–62} Recent developments in architectural engineering have allowed for synthesizing increasingly intricate polymer architectures, including star-shaped polymers. Star-shaped polymers are characterized by branched structures with multiple (>2) linear chains linked to a central point called the "core". Their simplicity in architectural deviation from linear polymers, higher-order architecture, and well-defined three-dimensional structure make them promising for designing and accessing advanced materials across diverse sectors such as electronics, medicine, and cosmetics.^{63–65} The branching of star polymers reduces polymer entanglement compared to their linear equivalents, distinguished by their compact structure and packing in the molten phase.^{66–69} Furthermore, other advantages include enhanced ultimate stress and toughness due to more pronounced strain hardening and superior strain recovery.^{70,71} Consequently, these advanced polymeric architectures hold significant promise in improving the processability of P3HB.

Although star architectures have been implemented for the ROP of various lactones and derivatives,⁷² reports detailing the synthesis of P3HB star homopolymers are scarce. In 2015, Mehrkhodavandi and coworkers reported the synthesis of three- and six-armed star-shaped P3HBs through the ROP of BBL using indium and zinc catalysts.⁷³ The resulting P3HBs are atactic to syndio-rich, with P_r (probability of *racemic* linkages between monomer units) values ranging around 0.55–0.62. Their study explored the effects of branching, highlighting improved packing of segments within a single chain. Additionally, Du and coworkers successfully generated multi-arm star-shaped P3HB from bio-based polyols through zinc-catalyzed ROP of BBL to produce atactic P3HB.⁷⁴ Nevertheless,

performance properties of such materials are compromised by the limitations in stereo control. Thus, there remains a need for achieving star-shaped P3HB polymers with enhanced tacticity as well as for investigating potential impacts of P3HB stereomicrostructures, when coupled with architectural variations, on their material properties.

Here, we report the synthesis and comprehensive characterization of 4-armed star-shaped P3HBs via ROP of 8DL^{Me} with a tetra-ol initiator for architectural control and yttrium catalysts for stereomicrostructural control. In this work, we showed that coupling architectural engineering with stereomicrostructural engineering can more effectively modulate the nucleation and crystallization ability of P3HB to improve the thermal, mechanical, and barrier properties of the resulting P3HB materials, as well as reducing their melt viscosities. The results highlight the potential of architectural manipulation to generate a diverse set of material properties for mono-material products.

Experimental Details

Materials

All syntheses and manipulations of air- and moisture-sensitive chemicals and materials were carried out in flamed-dried Schlenk-type glassware on a dual-manifold Schlenk line or in an inert gas (N₂)-filled glovebox. HPLC-grade organic solvents were first sparged extensively with nitrogen during filling 20 L solvent reservoirs and then dried by passage through activated alumina followed by passage through Q-5 supported copper catalyst (for toluene and hexanes) stainless steel columns. HPLC-grade dichloromethane (DCM) was stirred overnight over CaH₂ under N₂ and distilled under N₂ before use.

Yttrium chloride YCl₃ was purchased from Sigma-Aldrich Chemical Co. and used as received. Benzyl alcohol (BnOH) was purchased from Alfa Aesar, purified by stirring over CaH₂ overnight, distilled, then stored in the glovebox over activated Davison 4 Å molecular sieves. *N,N,N',N'*-tetrakis(2-hydroxyethyl)ethylenediamine was purchased from Sigma-Aldrich Chemical Co., purified by stirring over CaH₂ overnight, vacuum-distilled, and then stored in the glovebox. Dimethyl 1,4-dibenzyl-2,5-dioxocyclohexane-1,4-dicarboxylate was purchased from ThermoScientific and used as received. Iodomethane was purchased from Oakwood Chemical and used as received. Oxidant 3-chloroperoxybenzoic acid (*m*CPBA, ≤ 77%) was purchased from Sigma Aldrich and used as received. Literature procedures were employed for the preparation of *rac*- and *meso*-8DL^{Me} and sublimated twice before use for polymerizations.⁴⁵ Yttrium precursor, Y[N(SiHMe₂)₂]₃(THF)₂, and yttrium complexes were synthesized according to reported procedures.^{45,75,76}

Biological P3HB (*it*-P3HB_b) was purchased from Sigma-Aldrich (M_w (weight-average molar mass) = 437 kDa). Isotactic polypropylene (*it*-PP, 5 mm granules, M_n (number-average molar mass) = 97.0 kDa) was purchased from Sigma-Aldrich. Low-density polyethylene (LDPE, 3–4 mm granules, melt flow index



(MFI) = 7.5, Product Code INEOS LDPE 19N430) was purchased from INEOS Olefins & Polymers Europe, high-density polyethylene (HDPE, 2–4 mm granules, MFI = 7.6, Product Code ET32-GL-000110) was purchased from Goodfellow. Polybutylene adipate terephthalate (PBAT, M_w = 88.5 kDa) was purchased from BASF (Ecoflex F Blend C1200). All polymers were used as received.

General Polymerization Procedures

Polymerizations were performed in 7.0 mL glass reactors inside an inert N₂ glovebox at ambient temperature (~25 °C). The reactor was charged with a predetermined amount of monomer (8DL^{Me}) and solvent (DCM) in the glovebox, and a mixture of catalyst and initiator in solvent was stirred at ambient temperature for ~10 min in another reactor. The polymerization was initiated by rapid addition of the catalyst solution to the monomer solution. After a desired time, a 0.01 mL of aliquot was taken from the reaction mixture and quenched with a 5% solution of benzoic acid in CDCl₃ for ¹H-NMR analysis to obtain the percent monomer conversion data. The polymerization was then immediately quenched by addition of ~5 mL of HCl/MeOH (5% solution). The quenched mixture was then precipitated into an excess amount of cold methanol while stirring, filtered, washed with cold methanol to remove any unreacted monomer, and dried in a vacuum oven at 60 °C overnight to a constant weight. Larger scale reactions were performed in the same way but using a 50 mL glass reactor.

Instrumentation

Absolute Molar Mass Measurements. Measurements of polymer absolute M_w , M_n , and dispersity ($\bar{D} = M_w/M_n$) were performed via size exclusion chromatography (SEC). The SEC instrument consisted of an Agilent HPLC system equipped with one guard column and two PLgel 5 μ m mixed-C gel permeation columns and coupled with a Wyatt DAWN HELEOS II multi (18)-angle light scattering detector and a Wyatt Optilab TrEX dRI detector; the analysis was performed at 40 °C using chloroform as the eluent at a flow rate of 1.0 mL/min, using Wyatt ASTRA 7.1.2 molecular weight characterization software. Samples were run using the “assume 100 % mass recovery option” which calculated a dn/dc internally based on a precisely known polymer concentration of the sample prior to injection, which were 2.00–4.00 mg/mL.

Spectroscopic Characterizations. NMR spectra were recorded on a Bruker AV-III 400 MHz spectrometer (400 MHz, ¹H; 100 MHz, ¹³C) at 25 °C. Chemical shifts (δ) are reported in ppm with the solvent resonance employed as the internal standard (chloroform-*d*₁ at 7.26 ppm for ¹H NMR and 77.0 ppm for ¹³C NMR).

Thermal Analysis. Melting transition temperature (T_m), crystallization temperature (T_c), glass transition temperature (T_g), and heat of fusion (ΔH_f) were measured by differential scanning calorimetry (DSC) on an Auto Q20, TA Instrument. All T_m and T_g values were obtained from a second scan unless noted otherwise. Both

heating and cooling rates were 10 °C/min. Decomposition temperatures ($T_{d,5\%}$ defined by the temperature of 5% weight loss) and maximum rate decomposition temperatures (T_{max}) of the polymers were measured by thermal gravimetric analysis (TGA) on a Q50 TGA Analyzer, TA Instrument. Polymer samples were heated from ambient temperatures to 700 °C under N₂ at a heating rate of 10 °C/min. Values of T_{max} were obtained from derivative (wt %/°C) vs. temperature (°C) plots [derivative thermogravimetry (DTG)], while T_d were obtained from wt % vs. temperature (°C) plots.

Mechanical Analysis. Tensile stress/strain testing was performed by an Instron 5966 universal testing system (10 kN load cell) on dog-bone-shaped test specimens (ASTM D638 standard; Type V) prepared *via* compression molding using a Carver Auto Series Plus Laboratory Press (Carver, Model 3889.1PL1000, Max Force 15 ton) equipped with a two-column hydraulic unit (Carver, Model 3912, maximum force 24000 psi). Isolated polymer materials were loaded between non-stick Teflon paper sheets into a stainless-steel mold with inset dimensions 30 × 73.5 × 0.87 mm fabricated in house and compressed between two 6” × 6” steel electrically heated platens (EHPs) at a set pressure of 3000 psi, at temperature of each material’s respective T_m . Specimens for analysis were generated via compression molding and cut using an ASTM D638-5-IMP cutting die (Qualitest) to standard dimensions. Mechanical behavior was averaged for all the specimens measured for each individual species investigated. Thickness (0.38 ± 0.01 mm), width (3.18 mm), and grip length (26.4 ± 0.2 mm) of the measured dog-bone specimens were measured for normalization of data by the Bluehill Universal Software (TA). Test specimens were affixed into the screw-tight grip frame. Tensile stress and strain were measured to the point of material break at a grip extension speed of 5.0 mm/min at ambient conditions. Young’s modulus (E , MPa), stress at break or ultimate strength (σ_b , MPa), and elongation at break (ϵ_b , %) are obtained from the software analysis. Toughness values (U_T ; MJ m⁻³) were obtained by manual calculation (integration) of the area under the stress/strain curve.

The detailed tensile testing results of commercially available HDPE, LDPE, *it*-PP, and PBAT (individual stress/strain curves and tables) were previously reported, and the values were taken from that paper.^{77,78} Film processing (melt compression molding) was performed as previously indicated (*vide supra*). LDPE samples were heated to 110 °C. HDPE samples were heated to 150 °C. *it*-PP samples were heated at 175 °C. PBAT samples were heated to 135 °C. Tensile stress/strain tests were performed as previously indicated (*vide supra*).

Rheological Analysis. Rotational shear rheology experiments were performed on a Discovery Series Hybrid 2 (DHR-2) Rheometer (TA Instruments) in flow-sweep testing mode with a shear rate range of 10⁻³–10³ (1/s). Test specimens were trimmed at predetermined temperatures above the T_m . Polymer material was loaded between two 8 mm steel parallel-plate EHP geometries under N₂ (30 psi) gas flow and allowed to soak at specified temperatures for a minimum of 30 sec. Rheometer control and data analysis were performed with the TA Instruments TRIOS Software.



Polarized Light Optical Microscope Analysis. A polarized light optical microscope, Olympus BX51 (Olympus, Tokyo, Japan), equipped with an Olympus SC50 digital camera and with a Linkam-15 TP-91 hot stage (Linkam, Tadworth, U.K.; coupled to a liquid nitrogen cooling system) was used to observe the morphology of the samples, after crystallization from the melt. Films with around 100 μm thickness were prepared by melting the samples between two glass slides. The samples were heated to 190 $^{\circ}\text{C}$ or 135 $^{\circ}\text{C}$ to erase their thermal history, kept at this temperature for 1 min, and then were cooled from the melt at 20 $^{\circ}\text{C}/\text{min}$ to 25 $^{\circ}\text{C}$.

Successive Self-nucleation and Annealing (SSA). SSA is a thermal fractionation technique that is performed using a Differential Scanning Calorimetry (DSC) to study the different molecular segregation capacities that, normally, the semi-crystalline polymeric systems exhibit during isothermal crystallization and annealing processes. The SSA experiments were carried out following the protocol defined by Müller *et al.*⁵² The first heating scan is the one in which the thermal history of the sample is erased (heating the sample 20 $^{\circ}\text{C}$ above the melting point and keeping at that temperature for 3 minutes). For this work, during the second step the samples were cooled down at 20 $^{\circ}\text{C}/\text{min}$ to -30 $^{\circ}\text{C}$. After 1 min at this temperature, the sample is heated at the same rate to a temperature of 7.5 $^{\circ}\text{C}$ lower than the end-temperature melting (as a proxy of the ideal self-nucleation temperature)⁵² and kept for 3 min at that temperature (T_s). Subsequently, the sample was cooled again to -20 $^{\circ}\text{C}$ and held at this temperature for 1 min. This cyclic process was repeated by varying the T_s values 10 times, decreasing it at each cycle by 7.5 $^{\circ}\text{C}$. Finally, the sample was heated to the molten state (200 $^{\circ}\text{C}$ in this case) to observe the results of the SSA thermal fractionation. All the scans were performed at 20 $^{\circ}\text{C}/\text{min}$ in a Perkin Elmer DSC 8000 with an Intracooler II as a cooling system. This equipment was calibrated using indium and tin as standards.

Water Vapor Transmission Rate (WVTR). WVTR was measured using a modified version of ASTM E96/96M-16 (2016).⁷⁹ Standard 10 mL gas chromatography vials (Agilent Technologies, Santa Clara, CA) were used, each containing 7 mL of DI water. The film circles were sandwiched between two rubber sealing washers with outer and inner diameters of 20 mm and 9 mm, respectively. They were then placed on the vial openings and sealed using standard GC vial aluminum caps of 9 mm in diameter. Water vapor could only diffuse through the exposed circular area of the film. The sealed vials were then placed in an HPP 260 environmentally controlled oven (Mettler USA, Eagle, WI, USA) at 23 $^{\circ}\text{C}$ and 50 % relative humidity for 24 h to allow water absorption and achieve a steady diffusion state. After the conditioning period, the initial mass of each vial was measured, followed by 5 additional mass measurements over the next 120 h. Mass loss was plotted as a function of time, and the WVTR was determined from the slope of the obtained curve. All reported values are the average of 3 replicates. To obtain the water vapor permeability (WVP), the permeance was multiplied by the film thickness. The permeance was calculated by dividing the WVTR by the water vapor pressure difference (ΔP) across the film. ΔP was determined based on the saturation vapor pressure of water at the

test temperature (2812 Pa at 25 $^{\circ}\text{C}$) and the relative humidity difference (50%).

DOI: 10.1039/D5PY00691K

Results and Discussion

Synthesis of *it*-, *ir*-, and *sr*-star-shaped P3HB

This study employed monomers, *rac*-8DL^{Me} and *meso*-8DL^{Me},^{45,52,54} initiators, benzyl alcohol (BnOH) as the mono-initiator (**I_a**) for linear P3HB synthesis and *N,N,N',N'*-tetrakis(2-hydroxyethyl)ethylenediamine as the tetra-functional initiator (**I_b**) for star-P3HB synthesis due to its good solubility in dichloromethane (DCM), and pre-catalysts, yttrium salen complexes chosen for their steric openness and selectivity towards 8DL^{Me}.⁴⁵ Along with monomer and catalyst choices, the ratio between the catalyst and initiator is also important for achieving efficient polymerization. In the case of tetra-functional **I_b**, a 4:1 [**Y**] to [**I_b**] ratio is necessary to generate the corresponding four-armed yttrium alkoxide active propagating species via instantaneous alcoholysis of the yttrium complex. At the outset of this work, we showed that the initiation occurred at all four initiating sites of **I_b**, rather than mono, di-, or tri-initiation. Specifically, when pre-catalyst complex **1** was reacted with initiator **I_b** in different ratios (1:1, 2:1, 3:1, 4:1), ¹H-NMR showed intensity of the methylene peak next to the alcohol group, -CH₂-OH, decreased as the ratio was gradually increased and became unmeasurable when the ratio reached to 4:1 (Fig. S1), suggesting the formation of the active yttrium alkoxide species on each arm of the initiator. As simultaneous propagation of each of the four-armed alkoxide species is critical to generate discrete star-shaped P3HB, kinetic experiments were performed to interrogate the reactions of *rac*-8DL^{Me} with **1/I_b** and **1/I_a** in a *rac*-8DL^{Me}/catalyst/initiator ratio of 400:4:1 and 400:1:1. Since there are four propagation sites in the case of the **1/I_b** system for the star-P3HB synthesis, we observed its polymerization occurred faster than the **1/I_a** system for the comparative linear P3HB synthesis approximately by a factor of four, as evidenced by the slopes of the kinetic plots of the polymerization reactions: 0.22 for the linear polymer synthesis versus 0.83 for the star polymer synthesis (Fig. S2), all while maintaining low dispersity (\bar{D}), pointing to all four initiating sites propagating similarly.

The selection of catalyst allowed us to adjust the stereoselectivity of the polymerizations to achieve stereodiverse star-shaped P3HBs with medium to high molar mass ($M_n = 32.3$ to 208 kg mol⁻¹). Thus, upon optimization of reaction conditions, the ROP in a [*rac*-8DL^{Me}]/[**1**]/[**I_b**] ratio of 600:4:1 at room temperature (RT, ~25 $^{\circ}\text{C}$) achieved >99% monomer conversion in 10 min, affording high molar-mass isotactic four-armed star P3HB (*it*-s4-P3HB) with a low \bar{D} ($M_n = 204$ kg mol⁻¹, $\bar{D} = 1.15$; Table 1, Run 1). Incorporating bulky trityl (CPh₃) groups at the 3-position of the salicylic ligand framework leads to remarkable stereocontrol with $P_m > 0.99$ and [*mm*] (*meso* triads or isotacticity) > 99%, shown by {¹H} ¹³C NMR spectra where only one peak in each stereochemistry-diagnostic (methyl, methylene, and carbonyl) region was found (Figs. S3 and S4). To the best of our knowledge, this is the first report of highly isotactic star-P3HB. Of note is the distinctive aspect of this



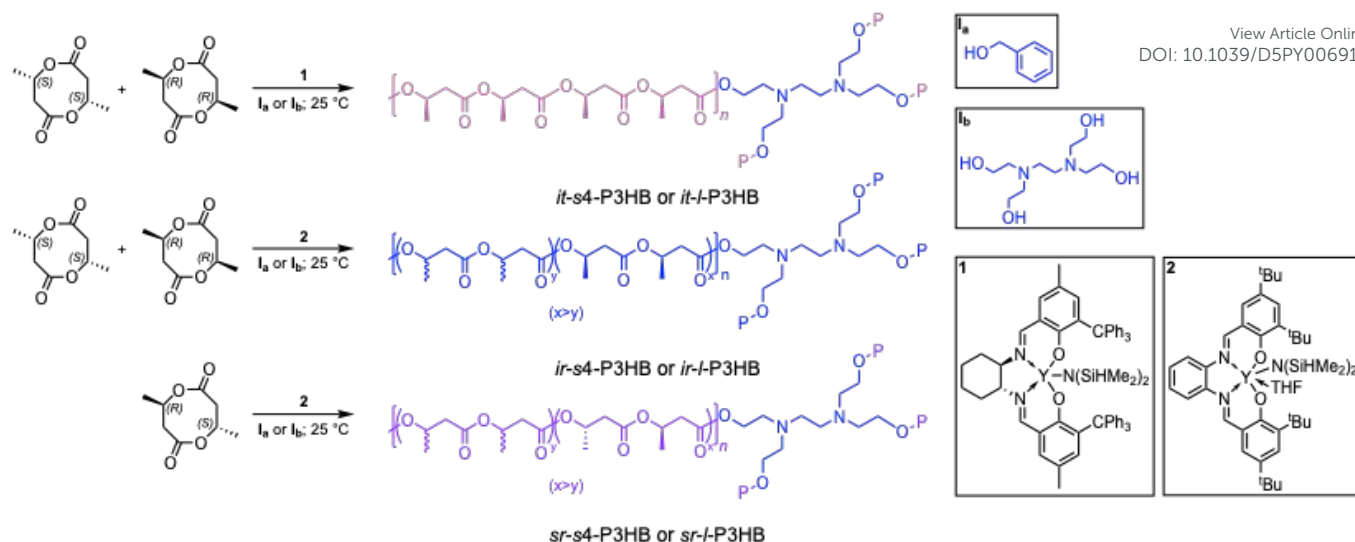


Figure 1. Overall reaction schemes for the synthesis of linear and star-shaped *it*-P3HB, *ir*-P3HB, and *sr*-P3HB.

polymerization system, which relies on employing a racemic catalyst (**1**, Figure 1). Upon mixing **1b** and racemic **1**, a total of 16 possible diastereomers of the propagating alkoxy catalyst could be generated from the instantaneous alcoholysis. Despite of this complexity, thanks to the exclusive enantioselectivity of the catalyst, that is, (*R,R*)-**1** selectively polymerizes (*S,S*)-8DL^{Me} while (*S,S*)-**1** selectively polymerizes (*R,R*)-8DL^{Me},⁴⁵ the ensuing polymerization produced quantitatively stereoregular *it*-P3HB. To further confirm the stereoselectivity outcome of this system, enantiopure (*R,R*)-**1** was also utilized in the ROP of *rac*-8DL^{Me} with **1b** (Table 1, Run 4; Scheme S1). This polymerization achieved 50% conversion, due to its exclusive selectivity to only polymerize (*S,S*)-8DL^{Me}, consistent with previous finding.⁴⁵ Moreover, the resulting enantiopure star-P3HB exhibited perfect isotacticity, as confirmed by ¹H ¹³C NMR (Fig.S7).

Next, we synthesized iso-rich and syndiorich-P3HB 4-armed stars, *ir*-s4-P3HB and *sr*-s4-P3HB, using **1b** and achiral pre-catalyst **2**. Specially, *ir*-s4-P3HB was synthesized from the ROP of *rac*-8DL^{Me} (Table 1, Run 5; Figure 1), while *sr*-s4-P3HB was synthesized in the same manner from the ROP of *meso*-8DL^{Me} (Table 1, Run 8; Figure 1). The ROP reactions were optimized in a [*rac*-8DL^{Me}]/[**2**]/[**1b**] ratio of 1000:4:1 (Table 1, Run 5) and a [*meso*-8DL^{Me}]/[**2**]/[**1b**] ratio of 750:4:1 (Table 1, Run 8) at RT, achieving >99% monomer conversion in 90 and 10 min, respectively. These polymerizations yielded high molar-mass *ir*-s4-P3HB ($M_n = 200 \text{ kg mol}^{-1}$, $\bar{D} = 1.23$) and *sr*-s4-P3HB ($M_n = 146 \text{ kg mol}^{-1}$, $\bar{D} = 1.27$). The stereomicrostructures of *ir*-s4-P3HB and *sr*-s4-P3HB were confirmed by ¹H ¹³C NMR analysis (Figs. S8-S13), showing [*mm*] (82%) and [*mr*] (18%) triad sequences with a P_m value of 0.91, and [*rr*] (58%) and [*mr*] (42%) triad sequences with a P_r value of 0.79, respectively.

Thermal Properties and Crystallization Behavior

DSC revealed a T_m of 168 °C for *it*-s4-P3HB, similar to the T_m of 171 °C observed in the linear counterpart (Table 1, Runs 1

and 2, Figs. S14 and S15). This high T_m renders it desirable for high-performance applications, resembling the characteristics observed for *it*-PP. It is noteworthy to highlight that the crystallinity of *it*-s4-P3HB appeared lowered by 11.3% in comparison to its linear counterpart ($X_c = 60.1\%$ determined by the degree of crystallinity; Table 1, Run 2) with a chain length approximately corresponding to the four arms, a phenomenon attributed to the polymer's slower crystallization.⁶⁰ Moreover, maintaining similar degradation temperatures to the linear analog, with a T_d of 254 °C and T_{max} of 281 °C, indicates that implementing architectural engineering does not compromise the thermal properties. However, *it*-P3HB has a higher T_m and a relatively low T_d that is only about 80 °C above its T_m , posing challenges for melt-processing due to its narrow processing window (difference between T_d and T_m).¹⁷

Installing a controlled amount of stereo-defects into the backbone of the polymer can effectively reduce their crystallinity and T_m values.^{52,53,80} Thus, *ir*-s4-P3HB (Table 1, Run 5) exhibits a lower T_m of 105 °C only observed in the 1st heating scan, accompanied by a lower degree of crystallinity ($X_c = 16.9\%$). With a similar T_d of 244 °C, *ir*-s4-P3HB exhibits a broader processing window of 139 °C compared to only 76 °C for *it*-l-P3HB (Table 1, Run 2). These results showed that the principle learned through our recent work on *sr*- and *ir*-P3HB can be readily applied here.^{52,53} We postulated the stereo-errors found in *ir*-s4-P3HB are randomly incorporated along the chain, interrupting the crystallization of the linear stereoregular chain segments and thereby lowering both the T_m and heat of fusion (ΔH_f). Likewise, *sr*-s4-P3HB exhibits a T_m of 123 °C, a $\Delta H_f = 21.4 \text{ J g}^{-1}$, and a T_d at 239 °C, which broadens the processing window up to 116 °C. Notably, both of these star polymers exhibit a lower degree of crystallinity compared to their linear counterparts (16.9 % vs. 30.1 % for *ir*-polymers and 14.7 % vs 21.1 % for *sr*-polymers).

To better understand the crystallizability differences between linear and star-shaped P3HBs, successive self-



Table 1. Selected results of the [Y]-catalyzed ROP of 8DL^{Me} with mono- and tetra-functional initiators ^aView Article Online
DOI: 10.1039/D5PY00691K

Run	[M]	Cat	[I]	Term	[M]/[cat]/ [I]	Time (min)	Conv. (%)	M_n^d (kg mol ⁻¹)	\bar{D}^d (M_w/M_n)	T_m^e (°C)	ΔH_f^f (J g ⁻¹)	X_c^g (%)	R_g^d (nm)	P_m^h	$T_{d,5\%}^i$ (°C)	T_{max}^i (°C)
1	<i>rac</i> -8DL ^{Me}	1	I _b	<i>it</i> -s4-P3HB	600/4/1	10	>99	204	1.15	168	71.2	48.8	22.1	>0.99	254	281
2	<i>rac</i> -8DL ^{Me}	1	I _a	<i>it</i> -I-P3HB	800/1/0.25	15	>99	208	1.01	171	87.8	60.1	68.7	>0.99	247	280
3	<i>rac</i> -8DL ^{Me}	1	I _a	<i>it</i> -I-P3HB (arm)	200/1/1 ^b	30	>99	32.3	1.07	160	77.5	53.1	n.d.	>0.99	233	262
4	<i>rac</i> -8DL ^{Me}	(R,R)-1	I _b	(S,S)- <i>it</i> -s4-P3HB	400/4/1 ^c	5	50	162	1.15	164/174	79.6	54.5	36.9	>0.99	263	284
5	<i>rac</i> -8DL ^{Me}	2	I _b	<i>ir</i> -s4-P3HB	1000/4/1	90	>99	200	1.23	105 ^f	24.7	16.9	31.3	0.91	244	240
6	<i>rac</i> -8DL ^{Me}	2	I _a	<i>ir</i> -I-P3HB	750/1/0.25	60	71	232	1.25	106 ^f	44.0	30.1	78.0	0.91	258	257
7	<i>rac</i> -8DL ^{Me}	2	I _a	<i>ir</i> -I-P3HB (arm)	250/1/1 ^b	15	>99	59.0	1.04	118 ^f	47.8	32.7	n.d.	0.91	262	291
8	<i>meso</i> -8DL ^{Me}	2	I _b	<i>sr</i> -s4-P3HB	750/4/1	10	>99	146	1.27	123	21.4	14.7	42.2	0.21	239	264
9	<i>meso</i> -8DL ^{Me}	2	I _a	<i>sr</i> -I-P3HB	800/1/0.5	35	>99	139	1.19	125	30.8	21.1	87.7	0.21	246	274
10	<i>meso</i> -8DL ^{Me}	2	I _a	<i>sr</i> -I-P3HB (arm)	150/1/1 ^b	15	>99	42.0	1.18	130	14.5	9.93	60.1	0.21	251	277

^a Conditions: 8DL^{Me} = 1.25 g (7.26 mmol) in DCM (7.26 mL), 1.0 M, ~25 °C, except for runs 3, 4, 7, and 10. ^b Conditions for runs 3, 7, and 10: 8DL^{Me} = 650 mg (3.76 mmol) in DCM (3.76 mL), 1.0 M, ~25 °C. ^c Conditions for run 4: 8DL^{Me} = 100 mg (0.58 mmol) in DCM (0.39 mL), 1.5 M, ~25 °C. ^d Determined by size exclusion chromatography (SEC) coupled with a Wyatt DAWN HELEOS II multi (18) angle light scattering detector and a Wyatt Optilab TrEX dRI detector and performed at 40 °C in chloroform. ^e Determined by DSC (10 °C/min) from second heating scans. ^f Determined by DSC (10 °C/min) from first heating scans. ^g See Supplementary Note 2. ^h Calculated from ¹³C NMR spectrum (CDCl₃, 23 °C). ⁱ Values obtained using thermogravimetric analysis (TGA) at a heating rate of 10 °C min⁻¹. n.d. = not determined.

nucleation and annealing (SSA) thermal fractionation studies were performed on all three-star polymers and their linear analogs for comparison purposes.^{81–84} Figure 2 shows the final DSC heating scans after applying the SSA protocol described in the Experimental Detail section. Figure 2A reveals *it*-P3HB polymers with the following differences: linear *it*-P3HB with a high M_n value (comparable to the M_n value of the *it*-s4-P3HB 4-arm star); linear *it*-P3HB with a lower M_n value (comparable to the M_n value of one of the arms of *it*-s4-P3HB, denoted as (arm)); and star *it*-s4-P3HB. These isotactic polymers were only slightly fractionated by SSA, meaning that only a few fractions are produced with a dominant large melting enthalpy fraction where most of the material melts in the range 160–180 °C. The highest M_n *it*-I-P3HB sample exhibited, as expected, the highest high-temperature melting fraction after SSA. In general, the low-temperature fractions are very small and broad.⁸⁵ The fractionated profile of the *it*-s4-P3HB sample is peculiar as it contains a small but high-temperature melting fraction (at ~174 °C), even though this is the sample with the lowest degree of crystallinity from those reported in Table 1, attributable to its star topology.

Stars have arms radiating from a common center group of atoms that do not enter the crystal lattice and are segregated into the amorphous regions. On the other hand, stars tend to have their arms in a more stretched-out conformation, which allows them to interdigitate with neighboring star chains. We postulate that this effect causes this high-temperature melting peak fraction. This result

could also indicate that star chains have a high level of interpenetration between them that could enhance percolation and, thus, mechanical properties, as explored in subsequent sections. As all the samples in Figure 2A are highly isotactic ($[mm] > 99\%$, see Table 1), the origin of the scarce SSA thermal fractionation can be ascribed mainly to their molar mass distribution and the intermolecular interactions present in these polymers. For the syndio-rich (*sr*) linear samples and the 4-arm sample in Fig 2.B, a much higher number of better-defined SSA thermal fractions were observed in comparison to the isotactic materials (Fig. 2A). It should also be noted that the melting range of the syndio-rich P3HB materials is lower in comparison to the isotactic materials. This increased capability of undergoing thermal fractionation in these syndio-rich materials is due to the much higher number of stereodefects that interrupt the linear crystallizable syndiotactic sequences along the chains ($[rr] = 58\%$, $[mr] = 42\%$, $P_r = 0.79$).⁸⁶ The stereo-defects also decrease the T_m of the material, as these defects limit the lamellar thickness that the polymer can achieve.

A similar result was obtained for *ir*-P3HB polymers (Fig. 2C), where a greater number of thermal fractions were observed in comparison to the *it*-P3HB samples, but fewer than in *sr*-materials. It should be noted that the T_m range for the *ir*-P3HB materials is lower than *sr*-P3HB samples. Although *ir*-P3HB polymers contain fewer stereodefects along the chain ($[mr]$ (18%) for *ir*-P3HB and (48%) for *sr*-P3HB), they appear less crystalline, as evidenced by the T_m



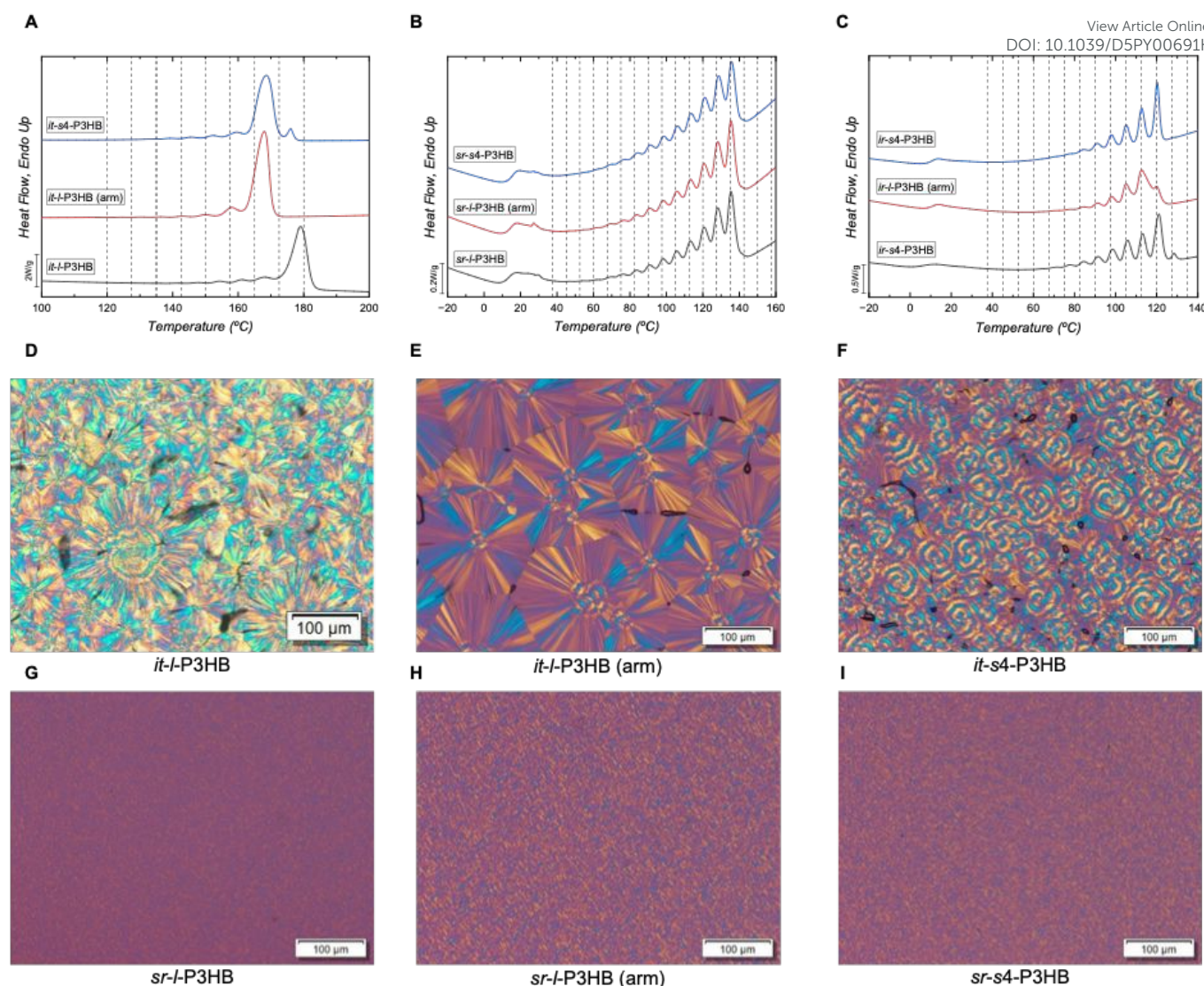


Figure 2. SSA and PLOM Properties of *it*-P3HB (*it*-s4-P3HB, *it*-l-P3HB, and *it*-l-P3HB (arm)) and *sr*-P3HB (*sr*-s4-P3HB, *sr*-l-P3HB, and *sr*-l-P3HB (arm)). The (arm) denotes the lower molar mass linear P3HB with the chain length equivalent of one arm of star-shaped P3HB.

observed only in the first heating scan. This difference is not due to a greater number of stereodefects but rather attributed to the inherent crystallinity differences of $[mm]$ and $[rr]$ triads. Specifically, $[rr]$ triads tend to form thicker, more crystalline lamellae that require higher melting temperatures, whereas $[mm]$ triads produce less crystalline structures with thinner lamellae, resulting in lower T_m and crystallinity. In fact, the quality of thermal fractionation, which refers to the degree of separation of each fraction (i.e., if each melting peak is well separated from its neighbors by having the valleys of the endothermic signals approaching the baseline in a higher degree) is also higher in the iso-rich materials.

Figure 2 panels D-I present the PLOM micrographs for the different P3HB samples studied here. All the samples underwent the same thermal treatment (heated to 190 °C or 135 °C and then cooled to 25 °C with a cooling ramp of 20 °C/min), and the images were taken after 12 h at 25 °C. All *it*-

P3HB samples exhibit large spherulites due to the low intrinsic nucleation density of *it*-P3HBs. Specifically, *it*-l-P3HB is characterized by forming large spherulites, as shown in Figure 2D and previously reported in the literature for bacterial and synthetic P3HB.⁵³ Reducing its M_n value produces, under the same thermal treatment, an increase in the spherulitic size and different optical properties. The micrographs in Figure 2E show the dominant positive character of the linear low M_n P3HB (*it*-l-P3HB (arm)) spherulites, consistent with previous reports of positive P3HB spherulites for similar materials.⁸⁶ On the other hand, the higher M_n sample (*it*-l-P3HB, Fig. 2D) exhibits a more mixed negative/positive character. The *it*-s4-P3HB shows slightly smaller average spherulitic size and double-banded spherulites (Fig. 2F). Banding has been attributed to lamellar twisting as lamellae grow radially inside the spherulites among other possibilities.^{87–89} It has also been reported that the spacing between bands tends to decrease with



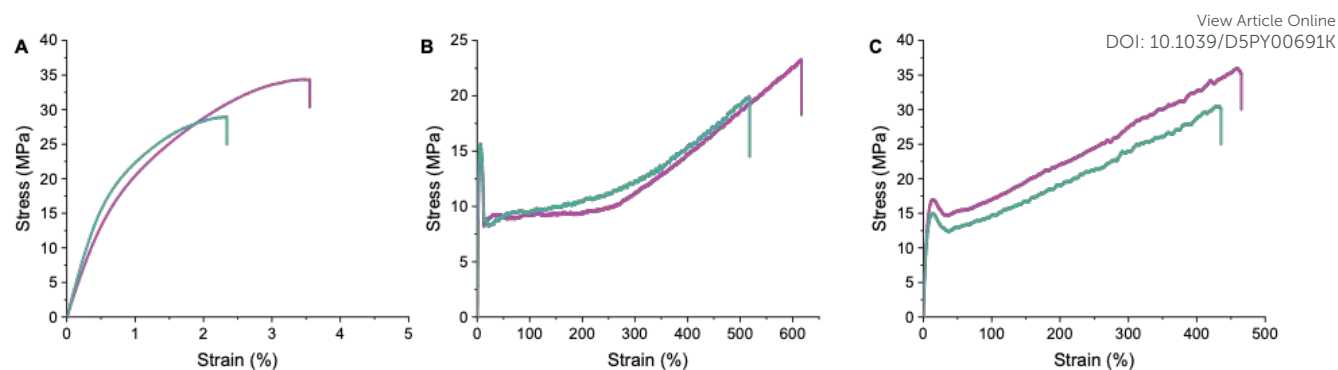


Figure 3. Tensile stress-strain plots of star-shaped P3HB (magenta) and linear P3HB (cyan curves): (A) *it*-s4-P3HB (magenta) and *it*-l-P3HB (cyan) overlays of representative stress-strain curves; (B) *ir*-s4-P3HB (magenta) and *ir*-l-P3HB (cyan) overlays of representative stress-strain curves; (C) *sr*-s4-P3HB (magenta) and *sr*-l-P3HB (cyan) overlays of representative stress-strain curves.

Table 2. Stress-strain data for Figure 3

Polymer Name	σ_B (MPa)	ϵ_B (%)	σ_Y (MPa)	ϵ_Y (%)	E (MPa)	U_T (MJ/m ³)
<i>it</i> -l-P3HB	29 ± 3	2 ± 0.2	-	-	3,670 ± 179	0.4 ± 0.1
<i>it</i> -s4-P3HB	34 ± 0.6	4 ± 0.3	-	-	2,933 ± 171	0.9 ± 0.1
<i>ir</i> -l-P3HB	19 ± 1	419 ± 25	15 ± 1	6 ± 0.4	715 ± 63	61 ± 7
<i>ir</i> -s4-P3HB	23 ± 1	603 ± 36	15 ± 1	7 ± 0.3	566 ± 27	83 ± 8
<i>sr</i> -l-P3HB	29 ± 2	419 ± 25	15 ± 0.2	14 ± 0.1	339 ± 4.9	84 ± 7
<i>sr</i> -s4-P3HB	35 ± 0.4	487 ± 33	16 ± 0.8	14 ± 0.1	349 ± 12	113 ± 7

supercooling, in the case of isothermal crystallization, but it can vary depending on non-isothermal conditions (i.e., cooling rates).⁸⁶ Therefore, P3HB may or may not show banding, depending on the thermal history and molar mass. On the other hand, *sr*-P3HB polymers are characterized by forming many small-sized spherulites, as observed in Figure 2 panels G-I. Stereodefects can increase the nucleation density of P3HB, as we have shown previously.^{52,53} The spherulitic size is small but visible under the PLOM, hence it should correspond to about 0.5 microns or larger. Finally, in the case of *ir*-P3HB polymers, no crystals were detected by PLOM, indicating that the spherulitic size must be smaller than the wavelength of light (400 nm) (Figs. S60-S62). The above results showed that star-shaped P3HBs exhibit a lower degree of crystallinity, smaller spherulites, and broader processing windows than their linear counterparts, making them well-suited for applications that demand enhanced thermal processability and controllable crystallinity.

Mechanical Properties

To test the hypothesis that combining stereo-defects with the modulation of architecture in star P3HB materials would lead to superior mechanical performance when compared to linear counterparts, we investigated their mechanical properties and compared them to their linear analogs of comparable molar mass, with representative stress strain curves plotted in Figure 3. Consistent with prior findings^{52,53}, introducing stereo-defects into the stereo-perfect *it*-P3HB backbone significantly enhances the mechanical

performance of P3HB: while linear and star-shaped *it*-P3HB materials are brittle (Fig. 3A), the addition of stereo-errors produces ductile P3HB materials that exhibit a yield point, neck formation, and strain propagation until breakage (Figs. 3B,C).

Across all three (*it*-, *ir*-, and *sr*-) P3HB sets, the star-shaped P3HBs consistently exhibited noticeably higher ultimate stress (σ_B) and elongation at break (ϵ_B) values than their linear counterparts, indicating an overall improvement in mechanical properties conferred by the star architecture (Table 2). In the case of *it*-P3HB, differences between the star and linear P3HB materials were minimal, though the star P3HB still showed marginally higher σ_B ($\sigma_B = 34 \pm 0.6$ vs. 29 ± 3 MPa) and slightly improved ϵ_B ($\epsilon_B = 4 \pm 0.3\%$ vs. $2 \pm 0.2\%$) vs. its linear counterpart (Tables S2 and S3; Figs. S47 and S48). Despite these differences, both materials remain brittle (Fig. 3A). More substantial improvements were observed in the ductile P3HB materials containing stereo-defects. More specifically, *ir*-s4-P3HB (Fig. 3B displayed a high ϵ_B ($\epsilon_B = 603 \pm 36\%$), a Young's modulus (E) of 566 ± 27 MPa, an σ_B of 23 ± 1 MPa, and a toughness (U_T) of 83 ± 8 MJ m⁻³, noticeably superior to its linear analog of comparable molar mass and arm molar mass (Tables S4-S6; Figures S49-S52). A similar trend was observed for *sr*-s4-P3HB (Fig. 3C; Tables S7-S9; Figs. S53-S56), where the star P3HB outperformed the linear analog in σ_B ($\sigma_B = 35 \pm 0.4$ vs. 29 ± 2 MPa) and toughness ($U_T = 113 \pm 7$ vs. 84 ± 7 MJ m⁻³). The percent changes in Table S12 quantify the relative differences between the star and linear polymers, with most properties exhibiting statistically significant increases for the



star polymers. A difference was considered meaningful when it exceeded the combined experimental uncertainty, calculated as described in the Supporting Information (Equations S1 and S2; Supplementary Note 1).

Increasing the number of arms in the star architecture from four to eight (i.e., 8-arm *sr*-P3HB) can further enhance tensile properties compared to 4-arm P3HB, as detailed in the Supporting Information (Scheme S2; Table S1, S10, S11; Figs. S57-S59). This improved performance could be attributed to the 8-arm structure that promotes more efficient stress distribution and energy dissipation under tensile stress. Unlike linear chains, which rely on entanglement density for mechanical strength, the branched architecture of star-shaped polymers distributes stress more uniformly, reducing localized stress points that can lead to fracture. The improved mechanical performance likely arises from multiple factors: decreased crystallinity allows enhanced ductility, and the core of the star structure acts as a permanent covalent crosslink, contributing to improved stiffness by distributing stress more evenly and preventing crack propagation under applied loads. These results are also related to those obtained in the PLOM micrographs, since all the *it*-P3HB materials with large spherulites (50-100 μm) are brittle. Such brittleness arises from a high degree of crystallinity and acute stress concentration in the interspherulitic regions, promoting fragility and earlier fracture propagation.^{53,90,91} Reducing the size of the spherulites by more than two orders of magnitude (below 0.5 μm) is a decisive factor together with the reduction in crystallinity to substantially improve mechanical properties and produce highly ductile materials.

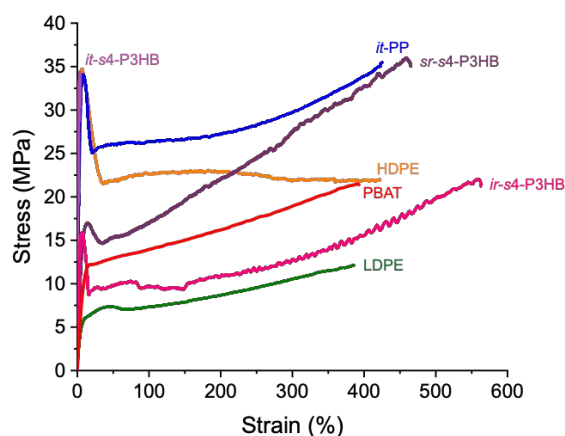


Figure 4. Stress-strain curve overlays of *it*-s4-P3HB, *ir*-s4-P3HB, and *sr*-s4-P3HB with commodity plastics including *it*-PP (blue), HDPE (orange), PBAT (red), and LDPE (green). Strain rate: 5.0 mm/min, ambient temperature.

The tensile properties of these three star-shaped P3HB materials were compared in Figure 4 to common commodity plastics including, HDPE, *it*-PP, and PBAT. While *it*-s4-P3HB is a brittle material, its stress at break (σ_B) is comparable to the yield stress (σ_Y) of *it*-PP. On the other hand, *ir*-s4-P3HB offers significantly higher ductility, and *sr*-s4-P3HB outperforms all

compared commodity plastics in overall mechanical performance, although its σ_Y is lower than that of HDPE and *it*-PP.

Rheological Properties

The challenges associated with melt-processing *it*-P3HB are well-documented, primarily attributed to its high T_m and low T_d , paired with high viscosity at high molar mass requiring high temperatures and/or high shear rates to process. Here, the branching structure plays a critical role in reducing polymer entanglement, potentially offering processing advantages over their linear equivalents. When compared to their linear analogues, star-shaped polymers have a smaller hydrodynamic volume and radius of gyration (R_g), as shown in Table 1, reflecting a more compact intramolecular packing within a single chain. This characteristic, coupled with reduced shear viscosity, contributes to improved melt-processability. Thus, a lower shear viscosity η would be observed for star polymers due to reduced entanglement density and improved chain alignment between polymer chains at moderate to high shear rates, resulting in an earlier and/or more pronounced shear thinning behavior.

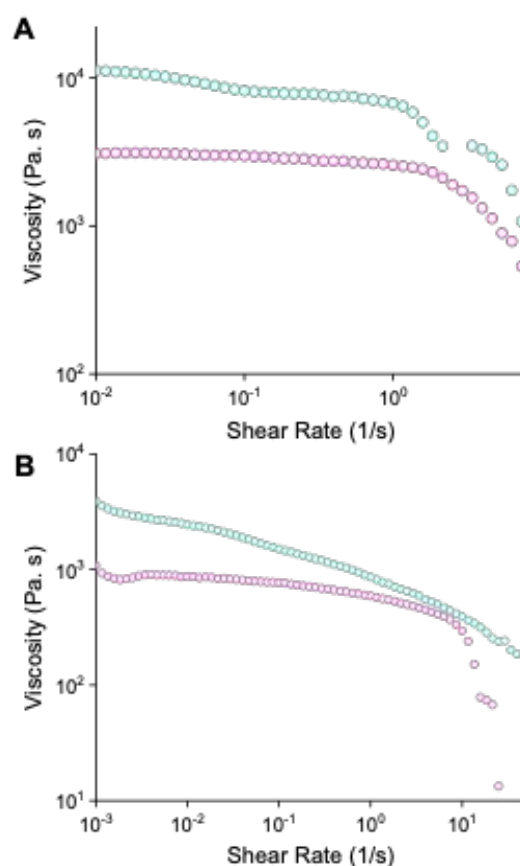


Figure 5. Rheological properties of star-shaped P3HB (magenta) and linear P3HB (cyan curves): (A) *ir*-s4-P3HB (magenta) and *ir*-l-P3HB (cyan) overlays of rotational shear rheology curves; (B) *sr*-s4-P3HB (magenta) and *sr*-l-P3HB (cyan) overlays of rotational shear rheology curves.



Accordingly, the rheological properties of the synthesized polymers were studied via rotational shear rheology at 1 Hz at +10 °C of the T_m of the studied polymer (115 °C for *ir*-P3HB and 135 °C for *sr*-P3HB). For the *ir*-P3HB, the star polymer, *ir-s4*-P3HB, showed a much lower initial melt viscosity (η_0^*) value of 3106 Pa·s than that of the linear analog, 10772 Pa·s (Fig. 5A). The same trend was observed for *sr*-P3HB: 1080 Pa·s for *sr-s4*-P3HB vs. 3877 Pa·s for the linear analog (Fig. 5B). Apart from the differences in melt viscosity, their shear rate-dependent behavior also differs. The star polymers exhibit a broader Newtonian plateau at low shear rates, which corresponds to a region where viscosity remains nearly constant despite changes in shear rate. In this regime, the polymer chains have sufficient time to relax between shear deformations so that the material behaves like a Newtonian fluid and its viscosity is independent of shear rate. In contrast, at higher shear rates, polymer chains begin to align in the direction of flow and cannot fully relax between deformations, which leads to shear thinning, where viscosity decreases as shear rate increases. Once shear thinning begins, the viscosity of the star polymers decreases much more rapidly than that of the linear analogs (Fig. 5A,B). This more pronounced shear thinning for the star P3HB suggests that at the high shear rates typically encountered in processing methods such as extrusion or injection molding, star polymers are more likely to flow and exhibit stronger shear thinning effects, making them more processable than linear analogs.

Barrier Properties

The synergistic coupling of high elastic modulus, high crystallinity, and excellent barrier properties of *it*-P3HB_b establish it as a compelling choice serving as a barrier layer in multi-layer packaging films.²⁴ To investigate the potential impact of the P3HB architecture on its barriers towards gas permeation, the barrier properties of *it-s4*-P3HB ($M_n = 152$ kg mol⁻¹, $\bar{D} = 1.22$), were investigated and compared to *it*-P3HB_b as well as selected commodity plastics HDPE and LDPE. For instance, commercially available, bacterial *it*-(*R*)-P3HB (Aldrich, $M_w = 437$ kDa) exhibits low water vapor transmission rate (WVTR) of 0.08 ± 0.005 g h⁻¹ m⁻² and a water permeance (WVP) of 5.1 ± 0.14 (g h⁻¹ s⁻¹ Pa⁻¹) × 10¹². While one might anticipate that *it-s4*-P3HB would have inferior barrier properties compared to *it*-linear P3HB due to its lower degree of crystallinity, its star-like structured architecture could potentially modify these properties. Indeed, the measured values of WVTR and WVP for *it-s4*-P3HB are 0.03 ± 0.013 g h⁻¹ m⁻² and 2.6 ± 0.68 (g h⁻¹ s⁻¹ Pa⁻¹) × 10¹² (Fig. 6), which showed comparable barrier properties to HDPE and LDPE (as judged by the WVP values) but superior barriers to its linear *it*-(*R*)-P3HB counterpart. We postulate that the distinctive architecture in star-shaped P3HB, characterized by a compact structure and increased intramolecular entanglements among the polymer arms, leads to reduced free volume, creating more tortuous paths

for gas diffusion and thus resulting in improved overall barrier properties.

DOI: 10.1039/D5PY00691K

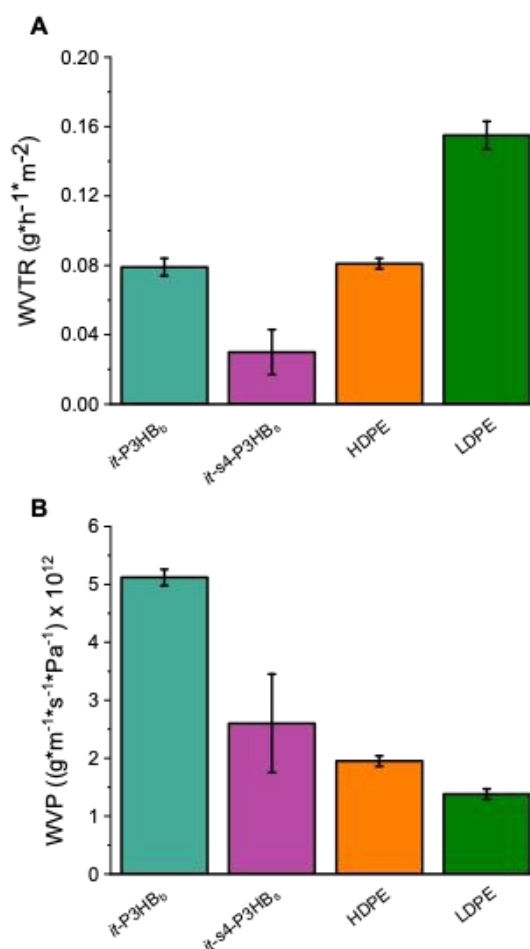


Figure 6. WVTR and WVP of *it*-P3HB_b, *it-s4*-P3HB ($M_n = 152$ kg mol⁻¹, $\bar{D} = 1.22$), and commodity plastics.

Conclusions

In summary, we have synthesized four-arm star-shaped P3HBs encompassing stereo-perfect isotactic stereomicrostructure to stereo-defected iso-rich and syndio-rich stereomicrostructures, *it-s4*-P3HB ($P_m > 0.99$), *ir-s4*-P3HB ($P_m = 0.91$), and *sr-s4*-P3HB ($P_r = 0.79$), as well as their linear counterparts of comparable molar mass as controls. Comprehensive, comparative characterization studies revealed various degrees of impacts of the P3HB architecture on thermal transitions, crystallization behavior, mechanical performance, rheological properties, and barrier properties. Notably, coupling the engineering of both stereomicrostructure and architecture has resulted in the synergistically enhanced impact on the overall materials properties of P3HB.

From the stereomicrostructure engineering perspective, the incorporation of stereo-defects in the polymer chains limits the crystallization of the materials and reduces the spherulitic sizes up to more than two orders of magnitude,



thereby improving mechanical properties. From the architecture perspective, having a higher ordered architecture such as the star-shaped P3HBs described herein, improves tensile strength, fracture strain, toughness, and melt-processability, as compared to their linear counterparts. Notably, the branching in the star-P3HB facilitates a denser packing of polymer chains, thereby reducing the free volume within the material. In essence, a more tightly packed structure can hinder the movement of gas molecules and improve its barrier properties to both water transmittance rate and permeance relative to its linear counterpart.

In a broader context, this work advances architectural engineering approaches towards mono-material design for plastic products, demonstrating the potential of engineering macromolecular architectures as an additional design tool for mono-materials. In particular, coupling of both stereomicrostructure and architecture engineering approaches provides a more powerful strategy to design plastics with vastly different, on-demand properties, all achievable without changing their chemical composition.

Author contributions

M.T.G.: investigation, data curation, writing – original draft, writing – review & editing, visualization, methodology, and validation. E.C.Q.: investigation, writing – review & editing, visualization, and methodology. F.S.: investigation, and data curation. J.L.O.: investigation, and data curation. S.X.: investigation. A.J.M.: resources, writing – review & editing, supervision, and project administration. E.Y.-X.C.: conceptualization, resources, writing – review & editing, supervision, project administration, and funding acquisition.

Corresponding authors: alejandrojesus.muller@ehu.es
eugene.chen@colostate.edu

Conflicts of interest

M.T.G., E.C.Q. and E.Y.-X.C. declare the following competing financial interest(s): A provisional patent (63/565,866) has been filed by Colorado State University Research Foundation on findings reported here. The rest of the authors declare no competing financial interests.

Data availability

+ The data supporting this article have been included as part of the Supplementary Information.

Acknowledgements

M.T.G., E.C.Q. and E.Y.-X.C. acknowledge support provided by the U.S. Department of Energy, Office of Energy Efficiency and Renewable Energy, Advanced Materials and Manufacturing Technologies Office (AMMTO), and Bioenergy Technologies

Office (BETO), performed as part of the BOTTLE Consortium, which includes the members from Colorado State University, and funded under contract no. DE-AC36-08GO28308 with the National Renewable Energy Laboratory, operated by the Alliance for Sustainable Energy. A.J.M, F.S. and J.L.O. acknowledge funding from the Basque Government through grant IT1503-22, and from the María de Maeztu Excellence Unit CEX2023-001303-M funded by MCIN/AEI/10.13039/501100011033.

References

- Geyer, R.; Jambeck, J. R.; Law, K. L. Production, Use, and Fate of All Plastics Ever Made. *Sci. Adv.*, 2017, **3**, e1700782.
- Nayanathara Thathsarani Pilapitiya, P. G. C.; Ratnayake, A. S. The World of Plastic Waste: A Review. *Cleaner Materials*, 2024, **11**, 100220.
- Xiang, Y.; Jiang, L.; Zhou, Y.; Luo, Z.; Zhi, D.; Yang, J.; Lam, S. S. Microplastics and Environmental Pollutants: Key Interaction and Toxicology in Aquatic and Soil Environments. *J. Hazard. Mater.*, 2022, **422**, 126843.
- Chae, Y.; An, Y. J. Current Research Trends on Plastic Pollution and Ecological Impacts on the Soil Ecosystem: A Review. *Environ. Pollut.*, 2018, **240**, 387–395.
- Lebreton, L.; Andrady, A. Future Scenarios of Global Plastic Waste Generation and Disposal. *Palgrave Commun.*, 2019, **5**, 1–11.
- Borrelle, S. B.; Ringma, J.; Lavender Law, K.; Monnahan, C. C.; Lebreton, L.; McGivern, A.; Murphy, E.; Jambeck, J.; Leonard, G. H.; Hilleary, M. A.; Eriksen, M.; Possingham, H. P.; De Frond, H.; Gerber, L. R.; Polidoro, B.; Tahir, A.; Bernard, M.; Mallos, N.; Barnes, M.; Rochman, C. M. Predicted Growth in Plastic Waste Exceeds Efforts to Mitigate Plastic Pollution. *Science*, 2020, **369**, 1515–1518.
- Andrady, A. L.; Neal, M. A. Applications and Societal Benefits of Plastics. *Philos. Trans. R. Soc. B, Biol. Sci.*, 2009, **364**, 1977–1984.
- Shi, C.; Reilly, L. T.; Phani Kumar, V. S.; Coile, M. W.; Nicholson, S. R.; Broadbelt, L. J.; Beckham, G. T.; Chen, E. Y.-X. Design Principles for Intrinsically Circular Polymers with Tunable Properties. *Chem.*, 2021, **7**, 2896–2912.
- Kwon, G.; Cho, D. W.; Park, J.; Bhatnagar, A.; Song, H. A Review of Plastic Pollution and Their Treatment Technology: A Circular Economy Platform by Thermochemical Pathway. *J. Chem. Eng.*, 2023, **464**, 142771.
- Epps, T. H.; Korley, L. T. J.; Yan, T.; Beers, K. L.; Burt, T. M. Sustainability of Synthetic Plastics: Considerations in Materials Life-Cycle Management. *J. Am. Chem. Soc. Au.*, 2022, **2**, 3–11.
- Samir, A.; Ashour, F. H.; Hakim, A. A. A.; Bassyouni, M. Recent Advances in Biodegradable Polymers for Sustainable Applications. *npj Mater. Degrad.*, 2022, **6**, 68.
- Singh, N.; Ogunseitan, O. A.; Wong, M. H.; Tang, Y. Sustainable Materials Alternative to Petrochemical Plastics Pollution: A Review Analysis. *Sustainable Horizons*, 2022, **2**, 100016.
- Rosenboom, J. G.; Langer, R.; Traverso, G. Bioplastics for a Circular Economy. *Nat. Rev. Mater.* 2022, **7**, 117–137.
- Moshood, T. D.; Nawanir, G.; Mahmud, F.; Mohamad, F.; Ahmad, M. H.; AbdulGhani, A. Biodegradable Plastic Applications towards Sustainability: A Recent Innovations in the Green Product. *Clean. Eng. Technol.*, 2022, **6**, 100404.



- 15 Sehgal, R.; Gupta, R. Polyhydroxyalkanoate and Its Efficient Production: An Eco-Friendly Approach towards Development. *3 Biotech.*, 2020, **10**, 549.
- 16 Meereboer, K. W.; Misra, M.; Mohanty, A. K. Review of Recent Advances in the Biodegradability of Polyhydroxyalkanoate (PHA) Bioplastics and Their Composites. *Green Chem.*, 2020, **22**, 5519–5558.
- 17 Westlie, A. H.; Quinn, E. C.; Parker, C. R.; Chen, E. Y.-X. Synthetic Biodegradable Polyhydroxyalkanoates (PHAs): Recent Advances and Future Challenges. *Prog. Polym. Sci.*, 2022, **134**, 101608.
- 18 Dilkes-Hoffman, L. S.; Lant, P. A.; Laycock, B.; Pratt, S. The Rate of Biodegradation of PHA Bioplastics in the Marine Environment: A Meta-Study. *Mar. Pollut. Bull.*, 2019, **142**, 15–24.
- 19 Müller, H. -M.; Seebach, D. Poly(Hydroxyalkanoates): A Fifth Class of Physiologically Important Organic Biopolymers? *Angew. Chem. Int. Ed.*, 1993, **32**, 477–502.
- 20 Muhammadi; Shabina; Afzal, M.; Hameed, S. Bacterial Polyhydroxyalkanoates-Eco-Friendly next Generation Plastic: Production, Biocompatibility, Biodegradation, Physical Properties and Applications. *Green Chem. Lett. Rev.*, 2015, **8**, 56–77.
- 21 Li, Z.; Yang, J.; Loh, X. J. Polyhydroxyalkanoates: Opening Doors for a Sustainable Future. *NPG Asia Mater.*, 2016, **8**, e265.
- 22 Sudesh, K.; Abe, H.; Doi, Y. Synthesis, Structure and Properties of Polyhydroxyalkanoates: Biological Polyesters. *Prog. Polym. Sci.*, 2000, **25**, 1503–1555.
- 23 Laycock, B.; Halley, P.; Pratt, S.; Werker, A.; Lant, P. The Chemomechanical Properties of Microbial Polyhydroxyalkanoates. *Prog. Polym. Sci.*, 2013, **38**, 536–583.
- 24 Sangroniz, A.; Zhu, J. B.; Tang, X.; Etxeberria, A.; Chen, E. Y.-X.; Sardon, H. Packaging Materials with Desired Mechanical and Barrier Properties and Full Chemical Recyclability. *Nat. Commun.*, 2019, **10**, 3559.
- 25 Tan, D.; Wang, Y.; Tong, Y.; Chen, G. Q. Grand Challenges for Industrializing Polyhydroxyalkanoates (PHAs). *Trends Biotechnol.*, 2021, **39**, 953–963.
- 26 Anjum, A.; Zuber, M.; Zia, K. M.; Noreen, A.; Anjum, M. N.; Tabasum, S. Microbial Production of Polyhydroxyalkanoates (PHAs) and Its Copolymers: A Review of Recent Advancements. *Int. J. Biol. Macromol.*, 2016, **89**, 161–174.
- 27 Wang, Y.; Yin, J.; Chen, G. Q. Polyhydroxyalkanoates, Challenges and Opportunities. *Curr. Opin. Biotechnol.*, 2014, **30**, 59–65.
- 28 Steinbüchel, A. Perspectives for Biotechnological Production and Utilization of Biopolymers: Metabolic Engineering of Polyhydroxyalkanoate Biosynthesis Pathways as a Successful Example. *Macromol. Biosci.*, 2001, **1**, 1–24.
- 29 Lenz, R. W.; Marchessault, R. H. Bacterial Polyesters: Biosynthesis, Biodegradable Plastics and Biotechnology. *Biomacromolecules*, 2005, **6**, 1–8.
- 30 Inoue, S.; Tomoi, Y.; Tsuruta, T.; Furukawa, J.; Gresham, T. L.; Jansen, J. E.; Shaver, F. W.; Amer, J. Organometallic-Catalyzed Polymerization of Propiolactone. *Die Makromolekulare Chemie.*, 1961, **48**, 229–233.
- 31 Tanahashi, N.; Doi, Y. Thermal Properties and Stereoregularity of Poly(3-Hydroxybutyrate) Prepared from Optically Active β -Butyrolactone with a Zinc-Based Catalyst. *Macromolecules.*, 1991, **24**, 5732–5733.
- 32 Agostini, D. E.; Lando, J. B.; Shelton, J. R. Synthesis and Characterization of Poly- β -Hydroxybutyrate. I. Synthesis of Crystalline DL-Poly- β -Hydroxybutyrate from DL- β -Butyrolactone. *J. Polym. Sci.*, 1971, **9**, 2775–2787.
- 33 Bloembergen, S.; Holden, D. A.; Bluhm, T. L.; Hamer, G. K.; Marchessault, R. H. Stereoregularity in Synthetic α -Hydroxybutyrate and γ -3-Hydroxyvalerate Homopolyesters. *Macromolecules.* 1989, **22**, 1656–1663.
- 34 Ajellal, N.; Durieux, G.; Delevoye, L.; Tricot, G.; Dujardin, C.; Thomas, C. M.; Gauvin, R. M. Polymerization of Racemic β -Butyrolactone Using Supported Catalysts: A Simple Access to Isotactic Polymers. *Chem. Commun.*, 2010, **46**, 1032–1034.
- 35 Mahrova, T. V.; Fukin, G. K.; Cherkasov, A. V.; Trifonov, A. A.; Ajellal, N.; Carpentier, J. F. Yttrium Complexes Supported by Linked Bis(Amide) Ligand: Synthesis, Structure, and Catalytic Activity in the Ring-Opening Polymerization of Cyclic Esters. *Inorg. Chem.*, 2009, **48**, 4258–4266.
- 36 Bruckmoser, J.; Pongratz, S.; Stieglitz, L.; Rieger, B. Highly Isolelective Ring-Opening Polymerization of Rac- β -Butyrolactone: Access to Synthetic Poly(3-Hydroxybutyrate) with Polyolefin-like Material Properties. *J. Am. Chem. Soc.*, 2023, **145**, 11494–11498.
- 37 Zintl, M.; Molnar, F.; Urban, T.; Bernhart, V.; Preishuber-Pflügl, P.; Rieger, B. Variably Isotactic Poly(Hydroxybutyrate) from Racemic β -Butyrolactone: Microstructure Control by Achiral Chromium(III) Salophen Complexes. *Angew. Chem. Int. Ed.*, 2008, **47**, 3458–3460.
- 38 Le Borgne, A.; Spassky, N. Stereoselective Polymerization of β -Butyrolactone. *Polymer (Guildf)*, 1989, **30**, 2312–2319.
- 39 Hori, Y.; Hagiwara, T. Ring-Opening Polymerisation of β -Butyrolactone Catalysed by Distannoxane Complexes: Study of the Mechanism. *Int. J. Biol. Macromol.*, 1999, **25**, 237–245.
- 40 Huang, H. Y.; Xiong, W.; Huang, Y. T.; Li, K.; Cai, Z.; Zhu, J. B. Spiro-Salen Catalysts Enable the Chemical Synthesis of Stereoregular Polyhydroxyalkanoates. *Nat. Catal.*, 2023, **6**, 720–728.
- 41 Arcana, M.; Giani-Beaune, O.; Schue, F.; Amass, W.; Amass, A. Structure and Morphology of Poly(β -Hydroxy-Butyrate) Synthesized by Ring-Opening Polymerization of Racemic (R,S)- β -Butyrolactone with Distannoxane Derivatives. *Polym. Int.*, 2000, **49**, 1348–1355.
- 42 Hori, Y.; Suzuki, M.; Yamaguchi, A.; Nishishita, T. Ring-Opening Polymerization of Optically Active β -Butyrolactone Using Distannoxane Catalysts: Synthesis of High Molecular Weight Poly(3-Hydroxybutyrate). *Macromolecules.*, 1993, **26**, 5533–5534.
- 43 Hörl, S.; Chiorescu, I.; Bruckmoser, J.; Futter, J.; Rieger, B. Influence of Ligand Design and Non-Covalent Interactions on the Isolelective Ring-Opening Polymerization of Rac- β -Butyrolactone Using Salan and Salalen Rare-Earth Metal Catalysts. *Angew. Chem. Int. Ed.*, 2025, **64**, e202504513.
- 44 Young, M. S.; LaPointe, A. M.; MacMillan, S. N.; Coates, G. W. Highly Enantioselective Polymerization of β -Butyrolactone by a Bimetallic Magnesium Catalyst: An Interdependent Relationship Between Favored and Unfavored Enantiomers. *J. Am. Chem. Soc.* 2024, **146**, 18032–18040.
- 45 Tang, X.; Chen, E. Y.-X. Chemical Synthesis of Perfectly Isotactic and High Melting Bacterial Poly(3-Hydroxybutyrate) from Bio-Sourced Racemic Cyclic Diolide. *Nat. Commun.*, 2018, **9**, 1–11.
- 46 Tang, X.; Westlie, A. H.; Caporaso, L.; Cavallo, L.; Falivene, L.; Chen, E. Y.-X. Biodegradable Polyhydroxyalkanoates by Stereoselective Copolymerization of Racemic Diolides: Stereocontrol and Polyolefin-Like Properties. *Angew. Chem. Int. Ed.*, 2020, **59**, 7881–7890.
- 47 Westlie, A. H.; Hesse, S. A.; Tang, X.; Quinn, E. C.; Parker, C. R.; Takacs, C. J.; Tassone, C. J.; Chen, E. Y.-X. All-Polyhydroxyalkanoate Triblock Copolymers via a



- Stereoselective-Chemocatalytic Route. *ACS Macro. Lett.*, 2023, **12**, 619–625.
- 48 Tang, X.; Shi, C.; Zhang, Z.; Chen, E. Y.-X. Toughening Biodegradable Isotactic Poly(3-Hydroxybutyrate) via Stereoselective Copolymerization of a Diolide and Lactones. *Macromolecules*, 2021, **54**, 9401–9409.
 - 49 Tang, X.; Shi, C.; Zhang, Z.; Chen, E. Y.-X. Crystalline Aliphatic Polyesters from Eight-Membered Cyclic (Di)Esters. *J. Polym. Sci.*, 2022, **60**, 3478–3488.
 - 50 Jaffredo, C. G.; Carpentier, J. F.; Guillaume, S. M. Poly(Hydroxyalkanoate) Block or Random Copolymers of β -Butyrolactone and Benzyl β -Malolactone: A Matter of Catalytic Tuning. *Macromolecules*, 2013, **46**, 6765–6776.
 - 51 Ajellal, N.; Thomas, C. M.; Carpentier, J. F. Functional Syndiotactic Poly(β -Hydroxyalkanoate)s via Stereoselective Ring-Opening Copolymerization of Rac- β -Butyrolactone and Rac-Allyl- β -Butyrolactone. *J. Polym. Sci. A. Polym. Chem.*, 2009, **47**, 3177–3189.
 - 52 Quinn, E. C.; Westlie, A. H.; Sangroniz, A.; Caputo, M. R.; Xu, S.; Zhang, Z.; Urgan-Demirtas, M.; Müller, A. J.; Chen, E. Y.-X. Installing Controlled Stereo-Defects Yields Semicrystalline and Biodegradable Poly(3-Hydroxybutyrate) with High Toughness and Optical Clarity. *J. Am. Chem. Soc.*, 2022, **45**, 5795–5802.
 - 53 Zhang, Z.; Quinn, E. C.; Olmedo-Martínez, J. L.; Caputo, M. R.; Franklin, K. A.; Müller, A. J.; Chen, E. Y.-X. Toughening Brittle Bio-P3HB with Synthetic P3HB of Engineered Stereomicrostructures. *Angew. Chem. Int. Ed.*, 2023, **62**, e202311264.
 - 54 Tang, X.; Westlie, A. H.; Watson, E. M.; Chen, E. Y.-X. Stereosequenced Crystalline Polyhydroxyalkanoates from Diastereomeric Monomer Mixtures. *Science*, 2019, **366**, 754–758.
 - 55 Zhang, Z.; Shi, C.; Scoti, M.; Tang, X.; Chen, E. Y.-X. Alternating Isotactic Polyhydroxyalkanoates via Site- and Stereoselective Polymerization of Unsymmetrical Diolides. *J. Am. Chem. Soc.*, 2022, **144**, 20016–20024.
 - 56 Zhou, L.; Zhang, Z.; Shi, C.; Scoti, M.; Barange, D. K.; Gowda, R. R.; Chen, E. Y.-X. Chemically Circular, Mechanically Tough, and Melt-Processable Polyhydroxyalkanoates. *Science*, 2023, **380**, 64–69.
 - 57 Quinn, E. C.; Knauer, K. M.; Beckham, G. T.; Chen, E. Y.-X. Mono-Material Product Design with Bio-Based, Circular, and Biodegradable Polymers. *One Earth*, 2023, **6**, 582–586.
 - 58 Butler, T.I., and Morris, B.A. 2016. Multilayer Flexible Packaging. Elsevier.
 - 59 Anukiruthika, T.; Sethupathy, P.; Wilson, A.; Kashampur, K.; Moses, J. A.; Anandharamakrishnan, C. Multilayer Packaging: Advances in Preparation Techniques and Emerging Food Applications. *Compr. Rev. Food. Sci. Food. Saf.*, 2020, **19**, 1156–1186.
 - 60 Ren, J. M.; McKenzie, T. G.; Fu, Q.; Wong, E. H. H.; Xu, J.; An, Z.; Shanmugam, S.; Davis, T. P.; Boyer, C.; Qiao, G. G. Star Polymers. *Chem. Rev.*, 2016, **116**, 6743–6836.
 - 61 Liffland, S.; Hillmyer, M. A. Enhanced Mechanical Properties of Aliphatic Polyester Thermoplastic Elastomers through Star Block Architectures. *Macromolecules*, 2021, **54**, 9327–9340.
 - 62 Liu, J.; Jia, M.; Gnanou, Y.; Feng, X. Heat-Resistant CO₂-Based Polycarbonate Thermoplastics. *Macromolecules*, 2024, **57**, 5380–5388.
 - 63 Wu, W.; Wang, W.; Li, J. Star Polymers: Advances in Biomedical Applications. *Prog. Polym. Sci.*, 2015, **46**, 55–85.
 - 64 Patil, R. A.; Aloorkar, N. H.; Kulkarni, A. S.; Ingale, D. J. Star Polymers: An Overview. *Int. J. Pharma. Nanotech. Res.* 2012, **5**, 1675–1684.
 - 65 Lapienis, G. Star-Shaped Polymers Having PEO Arms. *Prog. Polym. Sci.*, 2009, **34**, 852–892. DOI: 10.1039/D5PY00691K
 - 66 Chremos, A.; Douglas, J. F. Influence of Branching on the Configurational and Dynamical Properties of Entangled Polymer Melts. *Polymers (Basel)*, 2019, **11**, 1045.
 - 67 Giuntoli, A.; Chremos, A.; Douglas, J. F. Influence of Polymer Topology on Crystallization in Thin Films. *J. Chem. Phys.*, 2020, **152**, 044501.
 - 68 J. Roovers. Star and Hyperbranched Polymers; 1998.
 - 69 Dunstan, D. E. The Viscosity-Radius Relationship for Concentrated Polymer Solutions. *Sci. Rep.*, 2019, **9**, 1–9.
 - 70 Burns, A. B.; Register, R. A. Mechanical Properties of Star Block Polymer Thermoplastic Elastomers with Glassy and Crystalline End Blocks. *Macromolecules*, 2016, **49**, 9521–9530.
 - 71 Liffland, S.; Kumler, M.; Hillmyer, M. A. High Performance Star Block Aliphatic Polyester Thermoplastic Elastomers Using PDLA-b-PLLA Stereoblock Hard Domains. *ACS Macro Lett.*, 2023, 1331–1338.
 - 72 Cameron, D. J. A.; Shaver, M. P. Aliphatic Polyester Polymer Stars: Synthesis, Properties and Applications in Biomedicine and Nanotechnology. *Chem. Soc. Rev.*, 2011, **40**, 1761–1776.
 - 73 Ebrahimi, T.; Hatzikiriakos, S. G.; Mehrkhodavandi, P. Synthesis and Rheological Characterization of Star-Shaped and Linear Poly(Hydroxybutyrate). *Macromolecules*, 2015, **48**, 6672–6681.
 - 74 Omar, R.; Shaik, M.; Griggs, C.; Jensen, J. D.; Boyd, R.; Oncel, N.; Webster, D. C.; Du, G. Star-Shaped Poly(Hydroxybutyrate)s from Bio-Based Polyol Cores via Zinc Catalyzed Ring-Opening Polymerization of β -Butyrolactone. *Eur. Polym. J.*, 2021, **160**, 110756.
 - 75 Anwander, R.; Runte, O.; Eppinger, J.; Gerstberger, G.; Herdtweck, E.; Spiegler, M. Synthesis and Structural Characterisation of Rare-Earth Bis(Dimethylsilyl)Amides and Their Surface Organometallic Chemistry on Mesoporous MCM-41†. *J. Chem. Soc., Dalton Trans.*, 1998, **11**, 847–858.
 - 76 Liu, Q.; Meermann, C.; Görlitzer, H. W.; Runte, O.; Herdtweck, E.; Sirsch, P.; Törnroos, K. W.; Anwander, R. Cationic Rare-Earth Metal SALEN Complexes. *Dalton Trans.*, 2008, **44**, 6170–6178.
 - 77 Li, X. L.; Clarke, R. W.; Jiang, J. Y.; Xu, T. Q.; Chen, E. Y.-X. A Circular Polyester Platform Based on Simple Gem-Disubstituted Valerolactones. *Nat. Chem.*, 2023, **15**, 278–285.
 - 78 Sangroniz, A.; Sangroniz, L.; Aranburu, N.; Fernández, M.; Santamaria, A.; Iriarte, M.; Etxeberria, A. Blends of Biodegradable Poly(Butylene Adipate-Co-Terephthalate) with Poly(Hydroxi Amino Ether) for Packaging Applications: Miscibility, Rheology and Transport Properties. *Eur. Polym. J.*, 2018, **105**, 348–358.
 - 79 American Society for Testing and Materials. (2016). ASTM E96/E96M-16 Standard Test Methods for Water Vapor Transmission of Materials. In Annual Book of American Standard Testing Methods.
 - 80 Zhang, Z.; Quinn, E. C.; Kenny, J. K.; Grigoropoulos, A.; DesVeaux, J. S.; Chen, T.; Zhou, L.; Xu, T.; Beckham, G. T.; Chen, E. Y.-X. Stereomicrostructure-Regulated Biodegradable Adhesives. *Science*, 2025, **387**, 297–303.
 - 81 Müller, A. J.; Hernandez, Z. H.; Arnal, M. L.; Sanchez, J. J. Successive Self-Nucleation/Annealing (SSA): A Novel Technique to Study Molecular Segregation during Crystallization. *Polym. Bull.*, 1997, **39**, 465–472.
 - 82 Pérez-Camargo, R. A.; Cavallo, D.; Müller, A. J. Recent Applications of the Successive Self-Nucleation and Annealing Thermal Fractionation Technique. *Front. Soft Matter.*, 2022, **2**, 1003500.



- 83 Müller, A. J.; Michell, R. M.; Pérez, R. A.; Lorenzo, A. T. Successive Self-Nucleation and Annealing (SSA): Correct Design of Thermal Protocol and Applications. *Eur. Polym. J.*, 2015, **65**, 132–154.
- 84 Arnal, M. L.; Balsamo, V.; Ronca, G.; Sánchez, A.; Müller, A. J.; Cañizales, E.; Urbina De Navarro, C. APPLICATIONS OF SUCCESSIVE SELF-NUCLEATION AND ANNEALING (SSA) TO POLYMER CHARACTERIZATION. *J. Therm. Anal. Calorim.*, 2000, **59**, 451–470.
- 85 Sangroniz, L.; Jang, Y. J.; Hillmyer, M. A.; Müller, A. J. The Role of Intermolecular Interactions on Melt Memory and Thermal Fractionation of Semicrystalline Polymers. *J. Chem. Phys.*, 2022, **156**, 144902.
- 86 Caputo, M. R.; Tang, X.; Westlie, A. H.; Sardon, H.; Chen, E. Y.-X.; Müller, A. J. Effect of Chain Stereoconfiguration on Poly(3-Hydroxybutyrate) Crystallization Kinetics. *Biomacromolecules*, 2022, **23**, 3847–3859.
- 87 Xu, J.; Ye, H.; Zhang, S.; Guo, B. Organization of Twisting Lamellar Crystals in Birefringent Banded Polymer Spherulites: A Mini-Review. *Crystals*, 2017, **7**, 241.
- 88 Keith, H. D.; Padden, F. J. Banding in Polyethylene and Other Spherulites. *Macromolecules*, 1996, **29**, 7776–7786.
- 89 Lovinger, A. J. Twisted Crystals and the Origin of Banding in Spherulites of Semicrystalline Polymers. *Macromolecules*, 2020, **53**, 741–745.
- 90 Hou, X.; Sun, W.; Liu, Z.; Liu, S.; Yeo, J. C. C.; Lu, X.; He, C. Tailoring Crystalline Morphology via Entropy-Driven Miscibility: Toward Ultratough, Biodegradable, and Durable Polyhydroxybutyrate. *Macromolecules*, 2022, **55**, 5527–5534.
- 91 Eesaee, M.; Ghassemi, P.; Nguyen, D. D.; Thomas, S.; Elkoun, S.; Nguyen-Tri, P. Morphology and Crystallization Behaviour of Polyhydroxyalkanoates-Based Blends and Composites: A Review. *Biochem. Eng. J.*, 2022, **187**, 108588.

View Article Online
DOI: 10.1039/D5PY00691K



Data Availability Statement

View Article Online
DOI: 10.1039/D5PY00691K

The data supporting this article have been included as part of the Supplementary Information.

